High-accuracy determination of the ^{238}U/^{235}U fission cross section ratio up to ≈ 1 GeV at n_TOF at CERN

C. Paradela,[1,2] M. Calviani,[3] D. Tarrío,[1,4] E. Leal-Cidoncha,[1] L. S. Leong,[5,6] L. Tassan-Got,[5] C. Le Naour,[5] I. Duran,[1]
N. Colonna,[7,*] L. Audouin,[5] M. Mastromarco,[7] S. Lo Meo,[8] A. Ventura,[9] G. Aerts,[10] S. Altstadt,[11] H. Álvarez,[1]
F. Álvarez-Velarde,[12] S. Andriamonje,[10] J. Andrzejewski,[13] G. Badurek,[14] M. Barbagallo,[7] P. Baumann,[15] V. Bécares,[12]
F. Bečvář,[16] F. Belloni,[2] B. Berthier,[5] E. Berthoumieux,[10] J. Billowes,[17] V. Boccone,[3] D. Bosnar,[18] M. Brugger,[3] F. Calviño,[19]
D. Cano-Ott,[12] R. Capote,[20] C. Carrapiço,[21] P. Cennini,[3] F. Cerutti,[3] E. Chiaveri,[3] M. Chin,[3] G. Cortés,[22]
M. A. Cortés-Giraldo,[23] L. Cosentino,[24] A. Couture,[25] J. Cox,[25] S. David,[5] M. Diakaki,[26] I. Dillmann,[27] C. Domingo-Pardo,[28]
R. Dressler,[29] W. Dridi,[10] C. Eleftheriadis,[30] M. Embid-Segura,[12] L. Ferrant,[5] A. Ferrari,[3] P. Finocchiaro,[24] K. Fraval,[10]
K. Fujii,[31] W. Furman,[32] S. Ganesan,[33] A. R. García,[12] G. Giubrone,[28] M. B. Gómez-Hornillos,[22] I. F. Gonçalves,[21]
E. González-Romero,[12] A. Goverdovski,[34] F. Gramegna,[35] E. Griesmayer,[36] C. Guerrero,[3] F. Gunsing,[10] P. Gurusamy,[33]
R. Haight,[37] M. Heil,[27] S. Heinitz,[29] M. Igashira,[38] S. Isaev,[5] D. G. Jenkins,[39] E. Jericha,[36] Y. Kadi,[3] F. Käppeler,[40]
D. Karadimos,[41] D. Karamanis,[41] M. Kerveno,[15] V. Ketlerov,[34] N. Kivel,[29] M. Kokkoris,[26] V. Konovalov,[34] M. Krtička,[16]
J. Kroll,[16] C. Lampoudis,[30] C. Langer,[11] C. Lederer,[11] H. Leeb,[14] R. Losito,[3] M. Lozano,[23] A. Manousos,[30] J. Marganiec,[13]
T. Martínez,[12] S. Marrone,[7] C. Massimi,[42] P. Mastinu,[35] E. Mendoza,[12] A. Mengoni,[8] P. M. Milazzo,[31] F. Mingrone,[42]
M. Mirea,[43] W. Mondelaers,[2] C. Moreau,[31] M. Mosconi,[27] A. Musumarra,[44] S. O'Brien,[25] J. Pancin,[10] N. Patronis,[41]
A. Pavlik,[45] P. Pavlopoulos,[3] J. Perkowski,[13] L. Perrot,[10] M. T. Pigni,[14] R. Plag,[27] A. Plompen,[2] L. Plukis,[10] A. Poch,[19]
C. Pretel,[19] J. Praena,[23] J. Quesada,[23] T. Rauscher,[46,47] R. Reifarth,[11] A. Riego,[22] F. Roman,[3] G. Rudolf,[15] C. Rubbia,[3]
P. Rullhusen,[2] J. Salgado,[21] C. Santos,[21] L. Sarchiapone,[3] R. Sarmento,[21] A. Saxena,[33] P. Schillebeeckx,[2] S. Schmidt,[11]
D. Schumann,[29] C. Stephan,[5] G. Tagliente,[7] J. L. Tain,[28] L. Tavora,[21] R. Terlizzi,[7] A. Tsinganis,[3] S. Valenta,[16] G. Vannini,[42]
V. Variale,[7] P. Vaz,[21] R. Versaci,[3] M. J. Vermeulen,[39] D. Villamarin,[12] M. C. Vincente,[12] V. Vlachoudis,[3] R. Vlastou,[26] F. Voss,[27]
A. Wallner,[48] S. Walter,[27] T. Ware,[17] M. Weigand,[11] C. Weiß,[3] M. Wiesher,[25] K. Wisshak,[27] T. Wright,[17] and P. Žugec[18]
(n_TOF Collaboration)

^{1}*Universidade de Santiago de Compostela, Spain*
^{2}*European Commission JRC, Institute for Reference Materials and Measurements, Retieseweg 111, B-2440 Geel, Belgium*
^{3}*CERN, Geneva, Switzerland*
^{4}*Department of Physics and Astronomy, Uppsala University, Sweden*
^{5}*Centre National de la Recherche Scientifique/IN2P3 - IPN, Orsay, France*
^{6}*Japan Atomic Energy Agency, JAEA, Japan*
^{7}*Istituto Nazionale di Fisica Nucleare, Bari, Italy*
^{8}*ENEA, Bologna, Italy*
^{9}*Istituto Nazionale di Fisica Nucleare, Bologna, Italy*
^{10}*CEA/Saclay - IRFU, Gif-sur-Yvette, France*
^{11}*Johann-Wolfgang-Goethe Universität, Frankfurt, Germany*
^{12}*Centro de Investigaciones Energeticas Medioambientales y Tecnológicas (CIEMAT), Madrid, Spain*
^{13}*University of Lodz, Lodz, Poland*
^{14}*Atominstitut der Österreichischen Universitäten, Technische Universität Wien, Austria*
^{15}*Centre National de la Recherche Scientifique/IN2P3 - IReS, Strasbourg, France*
^{16}*Charles University, Prague, Czech Republic*
^{17}*University of Manchester, Oxford Road, Manchester, United Kingdom*
^{18}*Department of Physics, Faculty of Science, University of Zagreb, Croatia*
^{19}*Universidad Politecnica de Madrid, Spain*
^{20}*International Atomic Energy Agency (IAEA), Nuclear Data Section, Vienna, Austria*
^{21}*Instituto Superior Técnico/CTN, Universidade de Lisboa, Portugal*
^{22}*Universitat Politecnica de Catalunya, Barcelona, Spain*
^{23}*Universidad de Sevilla, Spain*
^{24}*INFN - Laboratori Nazionali del Sud, Catania, Italy*
^{25}*University of Notre Dame, Notre Dame, Indiana 46556, USA*
^{26}*National Technical University of Athens (NTUA), Greece*
^{27}*Forschungszentrum Karlsruhe GmbH (FZK), Institut für Kernphysik, Germany*
^{28}*Instituto de Física Corpuscular, CSIC-Universidad de Valencia, Spain*
^{29}*Paul Scherrer Institut, 5232 Villigen PSI, Switzerland*
^{30}*Aristotle University of Thessaloniki, Thessaloniki, Greece*
^{31}*Istituto Nazionale di Fisica Nucleare, Trieste, Italy*
^{32}*Joint Institute for Nuclear Research, Frank Laboratory of Neutron Physics, Dubna, Russia*
^{33}*Bhabha Atomic Research Centre (BARC), Mumbai, India*
^{34}*Institute of Physics and Power Engineering, Obninsk, Russia*

[35]*Istituto Nazionale di Fisica Nucleare, Laboratori Nazionali di Legnaro, Italy*

[36]*Atominstitut, Technische Universität Wien, Austria*

[37]*Los Alamos National Laboratory, Los Alamos, New Mexico 87545, USA*

[38]*Tokyo Institute of Technology, Tokyo, Japan*

[39]*University of York, Heslington, York, United Kingdom*

[40]*Karlsruhe Institute of Technology (KIT), Institut für Kernphysik, Karlsruhe, Germany*

[41]*University of Ioannina, Greece*

[42]*Dipartimento di Fisica, Università di Bologna, and Sezione INFN di Bologna, Italy*

[43]*Horia Hulubei National Institute of Physics and Nuclear Engineering - IFIN HH, Bucharest - Magurele, Romania*

[44]*Dipartimento di Fisica e Astronomia DFA, Università di Catania and INFN-Laboratori Nazionali del Sud, Catania, Italy*

[45]*University of Vienna, Faculty of Physics, Austria*

[46]*Centre for Astrophysics Research, School of Physics, Astronomy and Mathematics, University of Hertfordshire, Hatfield, United Kingdom*

[47]*Department of Physics, University of Basel, Basel, Switzerland*

[48]*Research School of Physics and Engineering, Australian National University, ACT 0200, Australia*

The ^{238}U to ^{235}U fission cross section ratio has been determined at n_TOF up to $\approx$1 GeV, with two different detection systems, in different geometrical configurations. A total of four datasets has been collected and compared. They are all consistent to each other within the relative systematic uncertainty of 3–4%. The data collected at n_TOF have been suitably combined to yield a unique fission cross section ratio as a function of neutron energy. The result confirms current evaluations up to 200 MeV. Good agreement is also observed with theoretical calculations based on the INCL++ /Gemini++ combination up to the highest measured energy. The n_TOF results may help solve a long-standing discrepancy between the two most important experimental datasets available so far above 20 MeV, while extending the neutron energy range for the first time up to $\approx$1 GeV.

I. INTRODUCTION

The neutron-induced fission cross section of the two major isotopes of uranium, ^{235}U and ^{238}U, are of fundamental importance in the field of nuclear technology, as well as for other fields of basic and applied nuclear physics. In particular, fission cross section data above a few MeV are important for the development of new systems for energy production and waste transmutation, for accelerator and space applications, in neutron flux measurements at high energies, or for the refinement of theoretical models on nuclear fission at high energy. The ^{235}U(n,f) cross section is a standard at 0.0253 eV and from 0.15 to 200 MeV [1,2], while ^{238}U(n,f) is a standard in the neutron energy region between 2 and 200 MeV [3]. While the ^{235}U(n,f) cross section is commonly used in a variety of fields, for example in neutron flux measurements, from thermal to very high energy, the ^{238}U(n,f) cross section can be more conveniently used in the presence of a low energy neutron background, thanks to its high fission threshold.

Despite its importance, few data have been collected up to now on the ^{238}U(n,f)/ ^{235}U(n,f) cross section ratio above 20 MeV. Lisowski *et al.* [4] measured the ratio at Los Alamos National Laboratory, from 0.5 to 400 MeV. Current evaluated nuclear data libraries [5] and evaluations of cross section

standards [1] are mostly based on these results. More recently, Shcherbakov *et al.* [6] measured the ratio between 1 and 200 MeV at the GNEIS facility, Gatchina. Above 50 MeV these results are between 5 and 8% lower than those of Lisowski *et al.*. On the contrary, results from Nolte *et al.* [7] seem to confirm the older measurement, but they are affected by a too large systematic uncertainty to draw a final conclusion. New, high-accuracy measurements are therefore required to solve the long-standing discrepancy, and improve the accuracy in current evaluations. An extension of the energy range up to higher energy would also be desirable, as data above 200 MeV could prove useful for refining theoretical models, in particular those used in modern Monte Carlo codes for high-energy neutron transport.

To address the need of new, accurate data for a future cross section standard, and to extend the current energy limit, a series of measurements of the ^{238}U(n,f)/ ^{235}U(n,f) cross section ratio were performed at the n_TOF facility at CERN, from 0.5 MeV to 1 GeV, in different experimental campaigns and with different setups. After a description of the various setups and analysis procedures in Sec. II, the n_TOF results are presented and compared with each other in Sec. III. Suitably combined in a unique dataset, the n_TOF results are then compared with previous experimental data, with current evaluations, and with the predictions of a theoretical model extending up to the highest measured energy. Conclusions are finally given in Sec. IV.

II. EXPERIMENTAL SETUP

The measurements were performed at the n_TOF facility at CERN [8–11], which is based on the spallation of 20 GeV/*c*

*nicola.colonna@ba.infn.it

protons on a Pb target. Data were collected in different experimental campaigns and with different experimental setups, taking advantage of the very convenient features of the neutron beam, that make this facility particularly suitable for measurements of neutron-induced fission cross sections [12]. In particular, the wide energy distribution of the neutron beam, extending over more than ten orders of magnitude, allows one to measure the fission cross section up to the GeV region. Furthermore, the long flight path, close to 200 m, ensured a good energy resolution at all energies.

The ^{238}U$(n,f)/\,^{235}$U(n,f) cross section ratio can be determined from the background-subtracted fission events $C(E_n)$, as a function of neutron energy, according to the following expressions:

$$\frac{\sigma_8(E_n)}{\sigma_5(E_n)} = \frac{C_8(E_n)}{C_5(E_n)} \times \frac{N_5}{N_8} \times \frac{\epsilon_5}{\epsilon_8} \times CF. \qquad (1)$$

Here the subscripts 8 and 5 refer to the ^{238}U(n,f) and ^{235}U(n,f) reactions, respectively, N is the areal density of the samples used in the measurements (in atoms/b), ϵ is the detection efficiency for fission events, and CF accounts for other corrections, in particular for the detection dead time. It is important to note that the ratio does not depend on either the shape or the absolute value of the neutron flux, since the two samples, having the same diameter, are measured simultaneously and in the same experimental setup, i.e., are exposed to the same neutron flux. As a consequence, the final uncertainties in the cross section ratio will mostly be determined by the uncertainty on the areal density of the two samples, and on the ratio of the efficiency and dead-time corrections.

The data reported here were collected with two detection systems: a fission ionization chamber (FIC), in which a single fission fragment (FF) is detected, and an array of parallel plate avalanche counters (PPACs), in which the two FFs are detected in coincidence. This last detection system was used in two geometrical configurations: one with the detectors mounted perpendicularly to the neutron beam direction, and the other (a tilted configuration) with the detectors at an angle of $45°$ relative to the neutron beam direction. A brief description of the detectors and other experimental details is given below for each setup, together with the systematic uncertainties affecting the corresponding results. All data here reported were collected with a large-aperture collimator (8 cm diameter). With such an arrangement, the beam profile is essentially flat over the surface of the samples, which were $\leqslant 8$ cm in diameter. This feature is of great advantage, since it minimizes the effect of possible inhomogeneities of the fissile deposit. Another important aspect of the n_TOF neutron beam regards the neutron energy resolution in the range reported here. Above a few MeV, this is dominated by the width of the proton beam, of 6 ns (r.m.s.). Considering the long flight path of 185 m, the energy resolution is better than 1% at 100 MeV, and reaches slightly over 5% at 1 GeV.

A. The FIC chamber

The fast ionization chamber (FIC) used in the measurement is described in detail in Ref. [13]. It is made of a stack of

ionization chambers mounted along the direction of the neutron beam. Each cell consists of a central aluminum electrode 100 μm thick, plated on both sides with the isotope to be measured, and two external 15-μm-thick aluminum electrodes. Different versions of the FIC were built. One of them, the FIC1, was specifically built for measurements of highly radioactive samples, and according to CERN regulations had to comply with the ISO2919 standard, as a "sealed source." For this reason, the case was made in stainless steel, and the chamber was equipped with thick stainless steel windows. The second version of the ionization chamber, FIC2, was much lighter and was directly coupled to the vacuum beam pipe, with only a 125-μm-kapton window at the gas/vacuum interface. For this reason, this second version was less sensitive to the so-called γ-flash, i.e., the prompt signal caused in the detector by spallation γ rays and relativistic particles. In both FIC1 and FIC2 chambers the gap between electrodes was 5 mm. All chambers were operated with a gas mixture of 90% Ar and 10% CF$_4$ at a pressure of 720 mbar. The detector signals were amplified by a current feedback operational amplifier AD844 and digitized with a flash analog-to-digital converter (FADC) with 8-bit resolution and 250 MHz sampling rate. The fast timing properties of the gas and of the front-end electronics resulted in a fast signal with a typical rise time of 40 ns and a fall time of 120 ns.

Two different measurements of the ^{238}U/^{235}U fission cross section ratio were performed with FIC1 and FIC2, respectively. In both measurements, the chambers were positioned at approximately 190 m downstream of the spallation target. In the measurement with FIC1, two ^{235}U and four ^{238}U samples were used. The samples were prepared by means of the painting technique at the Institute of Physics and Power Engineering, Obninsk, Russia, in form of the oxide U$_3$O$_8$. The isotopic purity was checked via α spectroscopy and was found to be better than 99% with only trace contaminations of other U isotopes. The nonuniformity of the samples was always between 5 and 10%. The deposit of fissile material was 8 cm in diameter, while the areal density of each sample was between 6×10^{-7} and 8×10^{-7} atoms/b, with a specified mass uncertainty of $\sim$1.3% (Table I). Due to a large γ-flash signal with a tail extending over a long time, it

TABLE I. List of samples used in the measurement with the fission ionization chambers. The samples in FIC1 and FIC2 were 8 and 5 cm in diameter, respectively.

Setup	Sample	Mass (mg)	Areal density (10^{-7} atoms/b)	Uncertainty (%)
	^{235}U	15.2	7.75	1.4
		16.6	8.46	1.3
FIC1	^{238}U	12.8	6.44	1.4
		12.4	6.24	1.4
		13.4	6.74	1.2
		13.7	6.90	1.4
	^{235}U	6.47	8.44	1.1
FIC2		6.32	8.25	1.1
	^{238}U	20.0	26.	>3

was not possible to collect useful data with this setup above 10 MeV. These results, on the other hand, are affected by a small systematic uncertainty on the mass of each sample, and possible inhomogeneities of the samples are averaged out when combining the different samples. Therefore, these data were used as the basis for the normalization of the second dataset, otherwise affected by larger systematic uncertainties, as explained below.

The second setup used in the measurement consisted of the FIC2 chamber, inside which two ^{235}U and one ^{238}U samples were mounted. All three samples were 5 cm in diameter. The areal density of the two ^{235}U samples was around 6×10^{-7} atoms/b, while a much thicker ^{238}U sample, of 2.6×10^{-6} atoms/b was used in this second setup, to collect sufficient statistics below the fission threshold as well. The uncertainty on the mass of this last sample was $>3\%$, and no information was available on the homogeneity of the deposit. For this reason, the data collected with this setup had to be normalized to the results obtained with the FIC1 chamber, in the 1–10 MeV neutron energy region. The characteristics of all samples used in the measurement with the fission ionization chamber are listed in Table I.

For the FIC2 chamber, an electronic compensation technique was applied in order to extract the FF signals from the tail of the γ-flash at short time-of-flights, i.e., for neutron energies above approximately 10 MeV. The technique is based on the observation that the shape of the γ-flash signal is similar for contiguous electrodes. Therefore, by subtracting the output of two consecutive electrodes, one of them without sample, it is possible to extract clear fission fragment signals. The presence of a residual tail related to the γ-flash required a more careful reconstruction procedure, with the threshold on the amplitude varying as a function of the neutron energy. The maximum energy reached with this procedure was around 200 MeV. More details on the performance of the detectors, in particular the separation between FF and α particles, can be found in Refs. [13,14].

In order to extract the neutron energy from the measured time-of-flight, a calibration was performed using the resonances in the ^{235}U(n,f) cross section. Corrections for the neutron beam attenuation in the samples and electrodes, and for the divergence of the beam profile, were estimated to be less than 1%, and were therefore neglected. Similarly, corrections for the sample inhomogeneities were considered negligible, in particular since the n_TOF neutron beam, for the large aperture collimator, shows a nearly flat spatial profile. Corrections had to be applied for the detection efficiency and for dead time effects. The efficiency corrections were applied only to the FIC1 data, which were used for normalization. The efficiency, estimated by means of detailed FLUKA simulations [15] of the energy deposition in the gas as a function of the threshold, was found to be 94.9% and 96.2% for the thin ^{235}U and ^{238}U samples mounted in FIC1, respectively. Contrary to the efficiency, dead-time corrections had to be applied to both FIC1 and FIC2 data, since they depend both on the sample and neutron energy. Such corrections, based on the nonparalyzable model, were below 5% in the whole neutron energy range for both thin samples, while it reached $\sim$10% for the thick ^{238}U sample used in FIC2.

B. The PPAC setup

At very high energies, the fission cross section measurements were carried out with the PPAC setup. The detectors, which are described in detail in Refs. [16,17], are characterized by very thin windows, small gaps between electrodes (3 mm) and low pressure of the gas. These features make the detector practically insensitive to the prompt γ-flash. Furthermore, the signals produced by the FF are very fast, less than 10 ns in width, so that the pile-up probability is very small. Most importantly, the very fast timing combined with the low sensitivity of the detectors to the γ-flash, allows one to record signals at very short time-of-flights, or equivalently at very high neutron energies, nominally up to 1 GeV.

A stack of PPACs was placed in the n_TOF beam for measuring FF in coincidence. The actinide samples were deposited on very thin backings and positioned between two PPACs. The main advantage of the coincidence technique is the very high efficiency for rejecting the α-particle background related to the natural radioactivity of the samples, as well as for discriminating fission against competing reactions, in particular high-energy neutron-induced reactions on the PPAC structural material, producing recoiling nuclei and charged particles inside the detectors. The performance of the PPACs, in particular in terms of discrimination of FF from α particles and other reaction products, and the fast recovery time of the γ-flash, are discussed in detail in Ref. [18]. Another advantage of PPACs is that they can also supply information on the angular distribution of fission fragments. Each cathode consists of 2-mm-wide strips to provide a one-dimensional position information. By combining the signals from orthogonal cathode strips, the fission fragment trajectory can be determined, allowing to reconstruct the emission angle. The main drawback of the system is a limited angular acceptance, since at relatively large angles one of the fragments loses a large fraction of its energy in the sample backing and in the entrance windows of the detectors, either being stopped before reaching the gas volume, or falling below the detection threshold. While the single fragment detection technique, used in the FIC detectors, is characterized by an efficiency for detecting the single fragment close to 100% (since the fragment has only to escape from the deposit of fissile material), in the coincidence technique the efficiency for grazing trajectories drops rapidly, going to zero for emission angles larger than $\sim$60$°$, the exact limiting angle depending on the thickness of the sample backing.

In the first experimental campaign at n_TOF the PPAC detectors were mounted in the neutron beam perpendicularly to the beam direction. Hereafter we will refer to this configuration as "PPAC perpendicular." In this configuration the setup is affected by a loss of efficiency for FF emitted at angles larger than $\sim$60$°$. To overcome the problem of the limited angular coverage, a new geometrical configuration was adopted at n_TOF in the second experimental campaign, with the detectors and the samples mounted at 45$°$ relative to the neutron beam direction. A scheme of the tilted configuration can be found in [17,19]. Two measurements were performed with the tilted setup, hereafter referred to as "PPAC tilted 1" and "PPAC tilted 2."

TABLE II. Characteristics of the samples used with the PPAC setup, both in the perpendicular configuration and in the first measurement with the tilted configuration ("PPAC tilted 1").

Sample	Mass (mg)	Areal density (10^{-7} atoms/b)	Uncertainty (%)
^{235}U	13.97	6.98	0.7
^{238}U	11.5	5.86	0.7

In all PPAC measurements the samples, prepared at IN2P3-Orsay, were 8 cm in diameter, with the fissile material electrodeposited on thin aluminum foils 2.0 and 0.7 μm in thickness in the first two and in the third measurement, respectively. The characteristics of the samples used in the first two cases are listed in Table II. The mass of the samples was determined by means of α counting. For the ^{235}U sample, the impurities were determined by mass spectrometry, which provided the atom ratios of 0.0628(1) and 7.472(15) $\times 10^{-3}$ for the ^{238}U/^{235}U and ^{234}U/^{235}U, respectively. The latter has been used to extract the total mass of ^{235}U from the measured α activity. The ^{238}U sample was of very high purity, as it was produced by magnetic separation from natural uranium. The homogeneity of the deposits was checked by α scanning, for the ^{235}U sample, and by Rutherford backscattering spectroscopy (RBS) for the ^{235}U and ^{238}U samples. RBS also provided the chemical composition of samples and backings. Apart from the contamination of ^{238}U in the ^{235}U sample, taken into account in the analysis, only trace concentrations of other isotopes were found in the samples (see Refs. [16,20]). The samples of the last measurement (PPAC tilted 2) have not been characterized with the necessary accuracy. As a consequence, this last dataset has been normalized to the ENDF/B-VII.1 evaluated ratio between 3 and 5 MeV.

In both configurations, a correction had to be applied for the loss of efficiency related to the stopping of one of the fission fragments in the sample backing. Because of the angular dependence of the efficiency, the fission fragment angular distribution (FFAD) had to be considered. To this end, corrections were calculated, by means of Monte Carlo simulations, on the basis of existing experimental results on the FFAD as a function of the neutron energy, reported in the EXFOR database for both isotopes [21]. More details on the procedure can be found in Refs. [16,20]. The FFAD is expressed as the sum of even Legendre polynomials in terms of the cosine of the emission angle (because of the forward-backward symmetry of the emitted FFs). In this work, polynomials up to second order only were considered, as there is no reliable information in literature about higher order coefficients. The energy-dependent coefficients were determined from the so-called anisotropy parameter, $A(E)$, defined as the ratio between the emission probability of the FF at 0 and 90°, $W(E,0°)/W(E,90°)$. The angular anisotropy of ^{235}U and ^{238}U was obtained by fitting the available literature data in the EXFOR database [21] up to ~20 and 100 MeV neutron energy in the case of ^{235}U and ^{238}U, respectively. Above those energies, the anisotropy was assumed to approach unity asymptotically. The data and the results of the fit are shown in Fig. 1.
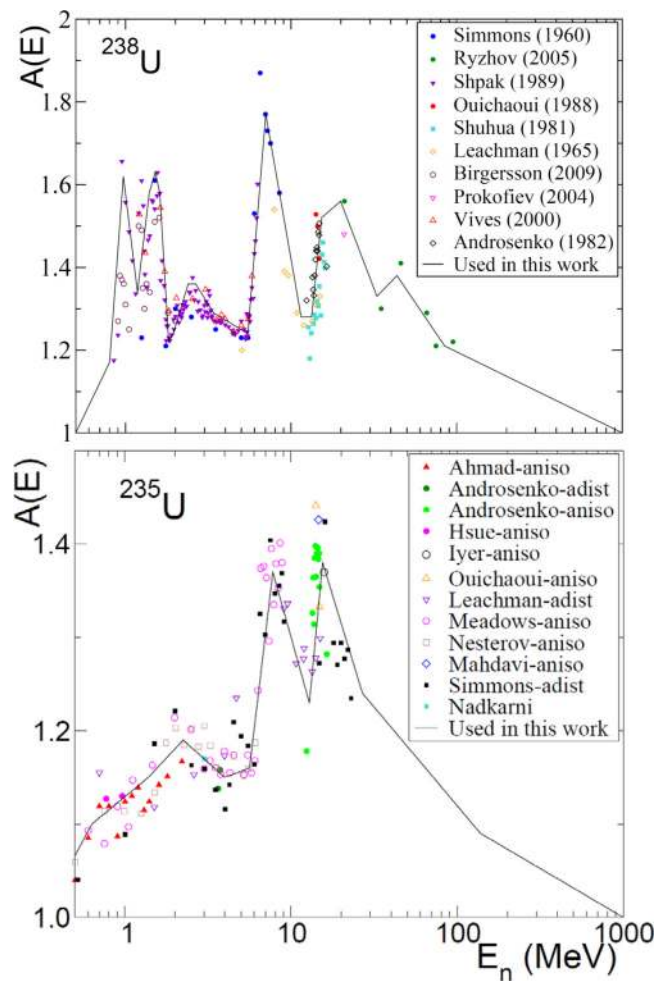
FIG. 1. (Color online) Anisotropy in the emission angle of FF in the neutron-induced fission of ^{238}U (upper panel) and ^{235}U (lower panel), as a function of the neutron energy. The curves represent the results of a fit of the various experimental data with Legendre polynomials.

FIG. 2. (Color online) Efficiency for detecting FFs in coincidence with the PPAC setup, in the two geometrical configurations. In the tilted setup, the gain of efficiency at large emission angles is compensated by a corresponding loss at all other angles.

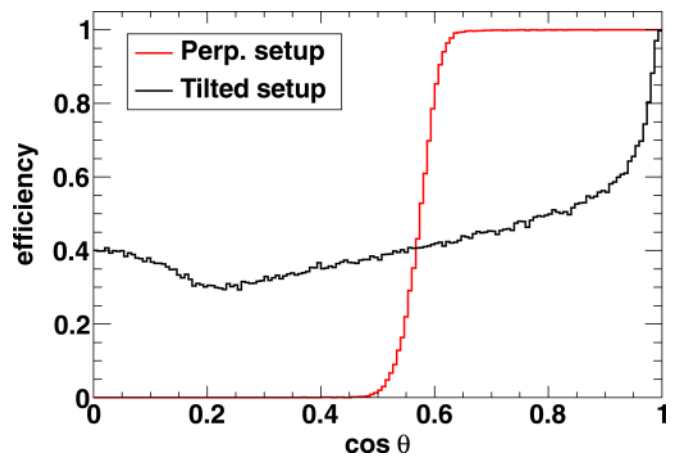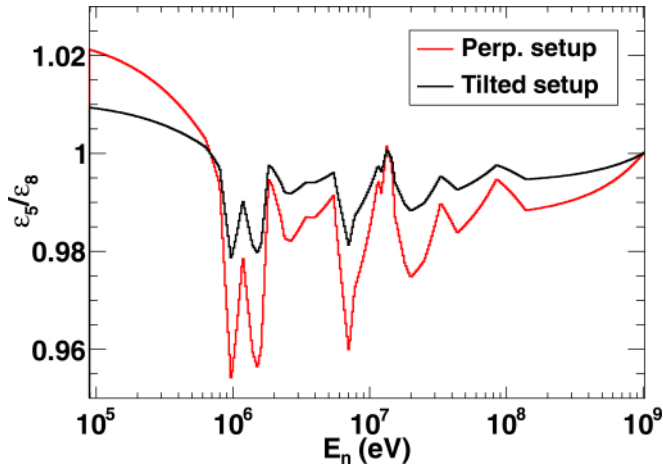FIG. 3. (Color online) Ratio between the efficiencies for detecting a fission event from the ^{235}U and ^{238}U samples respectively. The various structures in the efficiency ratio corresponds to the structures in the angular anisotropy of FF emission in the two reactions.
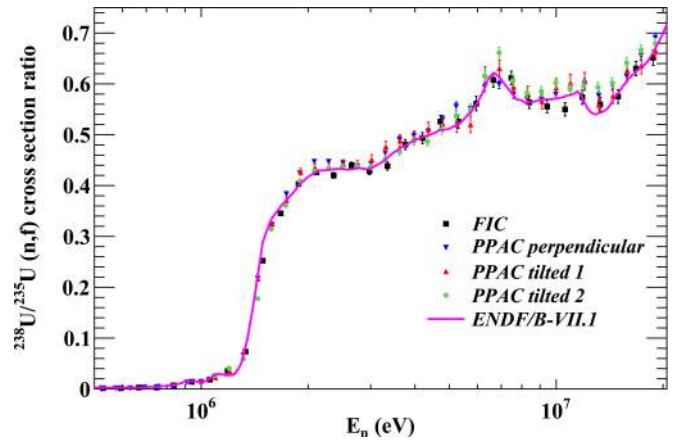

FIG. 4. (Color online) The ^{238}U/^{235}U fission cross section ratio measured at n_TOF with the different setups, in the neutron energy range 500 keV - 20 MeV. The error bars represent only the statistical uncertainties. For comparison, the ratio calculated on the basis of the evaluated cross sections from ENDF/B-VII.1 is also shown in the figure (solid line).

The detection efficiency of the PPAC setup as a function of the FF emission angle is shown in Fig. 2 for the perpendicular and tilted configurations. The figure clearly shows the difference between the two configurations: in the perpendicular case, the efficiency is flat up to a given angle (around $\sim 60°$), and drops to zero above this limit. On the contrary, in the tilted configuration all FF emission angles are covered. The gain in efficiency at large angles is obviously compensated by a reduction of the efficiency at smaller angles, due to the cut in the azimuthal angle related to the stopping of the fragments in the dead layers (sample backing and PPAC windows). As expected, the global efficiency, i.e., the efficiency integrated over the polar angle, is nearly the same in both perpendicular and tilted configuration, but the latter has the advantage of a smaller influence of the angular anisotropy of FF emission.

The analysis of the tilted configuration is described in great detail in Refs. [17,22,23]. Several conditions were applied in order to identify the fission fragments, reconstruct the trajectory of each fragment, and reject all possible sources of background. The efficiency corrections obtained by Monte Carlo simulations [22] were confirmed by means of a method based exclusively on experimental data [23]. Contrary to the

perpendicular configuration, a dependence of the efficiency on the polar angle has to be taken into account, together with other effects related to the viewing angle of the sample by the detectors.

As shown in Eq. (1), the cross section ratio depends on the ratio of the efficiency for detecting a fission event from the ^{235}U and the ^{238}U samples respectively. The ratio is shown in Fig. 3, for the two different configurations. In both cases, the correction is of at most 4%. The systematic uncertainties affecting the various PPAC measurements, as well as the measurement with the FIC, are listed in Table III.

III. RESULTS AND DISCUSSION

Figure 4 shows the results of the different measurements of the ^{238}U/^{235}U fission cross section ratio, for neutron energies in the range 500 keV–20 MeV. For comparison, the ratio extracted from the ENDF/B-VII.1 evaluated cross sections is

TABLE III. Systematic uncertainties (in %) on the data collected in the four different measurements of the ^{238}U/^{235}U fission cross section ratio. "Others" refers to dead-time corrections. Since the same samples were used in the second and third measurement, the corresponding uncertainties on the sample mass are fully correlated. For the last dataset, normalized to ENDF/B-VII.1, the uncertainty in the mass is replaced by the one in the evaluated cross sections.

Setup	Samples	Efficiency	Others	Total
FIC	2	1	3	3.5
PPAC perpend.	1.1	3	<1	$\gtrsim 3$
PPAC tilted 1	1.1	2	<1	$\lesssim 3$
PPAC tilted 2	(~ 1)	1	<1	2.5

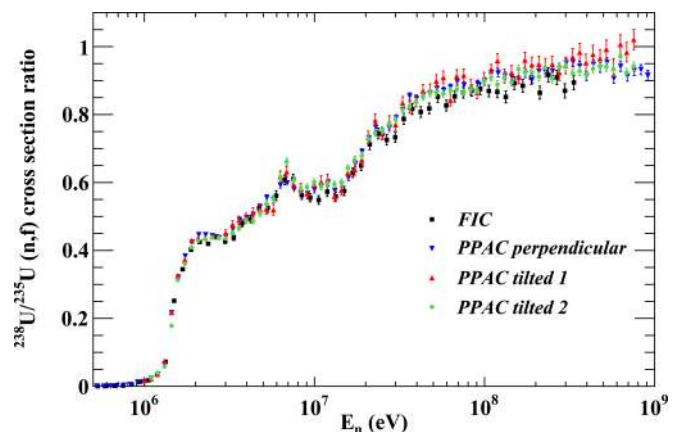
FIG. 5. (Color online) The ^{238}U/^{235}U fission cross section ratio from the different n_TOF measurements, in the neutron energy range 500 keV–1 GeV.

TABLE IV. ^{238}U/ ^{235}U fission cross section ratio determined at n_TOF in four different measurements, as function of the neutron energy (in MeV). E_{low} and E_{high} refer to the lower and upper limit of the neutron energy bin, respectively. The number in parentheses represents only the uncertainty related to counting statistics. In the last column the weighted average of the four measurements is reported.

E_{low}	E_{high}	FIC	PPAC Perp.	PPAC tilted 1	PPAC tilted 2	$\langle n\_TOF\rangle$
0.661	0.724	0.002(0)	0.002(0)			0.002(0)
0.724	0.794	0.002(0)	0.003(0)			0.003(0)
0.794	0.871	0.006(1)	0.005(0)			0.005(0)
0.871	0.955	0.012(1)	0.012(1)			0.012(0)
0.955	1.047	0.015(1)	0.014(1)	0.015(1)	0.000(0)	0.014(0)
1.047	1.148	0.023(1)	0.024(1)	0.023(1)	0.024(1)	0.024(0)
1.148	1.259	0.035(1)	0.035(1)	0.035(2)	0.039(1)	0.036(1)
1.259	1.380	0.061(2)	0.066(1)	0.074(2)	0.057(1)	0.063(1)
1.380	1.514	0.197(3)	0.216(2)	0.217(4)	0.176(3)	0.202(1)
1.514	1.660	0.310(4)	0.321(3)	0.325(5)	0.313(3)	0.318(2)
1.660	1.820	0.363(5)	0.383(3)	0.372(6)	0.359(4)	0.371(2)
1.820	1.995	0.407(5)	0.424(3)	0.427(6)	0.407(4)	0.417(2)
1.995	2.188	0.425(6)	0.446(4)	0.436(7)	0.428(4)	0.436(2)
2.188	2.399	0.419(6)	0.446(4)	0.436(7)	0.433(4)	0.436(2)
2.399	2.630	0.430(6)	0.443(4)	0.443(7)	0.436(5)	0.439(3)
2.630	2.884	0.439(7)	0.437(4)	0.441(8)	0.436(5)	0.438(3)
2.884	3.162	0.426(7)	0.442(5)	0.451(9)	0.435(6)	0.438(3)
3.162	3.467	0.435(8)	0.463(6)	0.477(11)	0.450(7)	0.455(4)
3.467	3.802	0.469(10)	0.490(6)	0.488(12)	0.465(8)	0.479(4)
3.802	4.169	0.486(10)	0.496(7)	0.496(12)	0.486(8)	0.492(4)
4.169	4.571	0.502(11)	0.506(7)	0.511(13)	0.486(9)	0.500(5)
4.571	5.012	0.526(12)	0.529(8)	0.522(14)	0.509(9)	0.522(5)
5.012	5.495	0.524(13)	0.555(9)	0.520(16)	0.536(10)	0.540(6)
5.495	6.026	0.546(14)	0.550(9)	0.520(16)	0.549(11)	0.545(6)
6.026	6.607	0.587(14)	0.592(9)	0.617(17)	0.615(11)	0.600(6)
6.607	7.244	0.615(14)	0.598(8)	0.631(16)	0.660(10)	0.621(5)
7.244	7.943	0.607(13)	0.579(8)	0.594(15)	0.605(10)	0.593(5)
7.943	8.710	0.566(13)	0.569(8)	0.581(15)	0.581(9)	0.573(5)
8.710	9.550	0.556(12)	0.568(8)	0.566(15)	0.584(10)	0.570(5)
9.550	10.471	0.549(12)	0.578(9)	0.594(16)	0.600(10)	0.581(5)
10.471	11.482	0.555(13)	0.587(9)	0.602(17)	0.588(10)	0.583(6)
11.482	12.589	0.573(14)	0.600(9)	0.605(17)	0.595(10)	0.595(6)
12.589	13.804	0.560(14)	0.576(9)	0.559(16)	0.593(10)	0.577(6)
13.804	15.136	0.564(14)	0.596(9)	0.576(15)	0.600(10)	0.590(5)
15.136	16.596	0.604(14)	0.614(9)	0.627(16)	0.641(10)	0.622(6)
16.596	18.197	0.636(14)	0.655(9)	0.636(17)	0.666(10)	0.653(6)
18.197	19.953	0.654(15)	0.690(9)	0.665(17)	0.678(10)	0.677(6)
19.953	21.878	0.706(16)	0.730(10)	0.733(18)	0.728(11)	0.726(6)
21.878	23.988	0.741(16)	0.762(10)	0.782(18)	0.744(10)	0.755(6)
23.988	26.303	0.737(16)	0.738(9)	0.742(17)	0.752(10)	0.743(6)
26.303	28.840	0.722(15)	0.760(9)	0.778(18)	0.771(10)	0.760(6)
28.840	31.623	0.737(15)	0.790(10)	0.770(17)	0.784(10)	0.777(6)
31.623	34.674	0.782(16)	0.814(10)	0.834(18)	0.814(10)	0.812(6)
34.674	38.019	0.813(16)	0.854(10)	0.822(18)	0.824(10)	0.834(6)
38.019	41.687	0.814(16)	0.847(10)	0.841(18)	0.836(10)	0.838(6)
41.687	45.709	0.806(16)	0.858(10)	0.870(18)	0.852(10)	0.849(6)
45.709	50.119	0.822(16)	0.863(10)	0.871(18)	0.863(10)	0.858(6)
50.119	54.954	0.852(16)	0.876(10)	0.898(19)	0.865(10)	0.871(6)
54.954	60.256	0.833(16)	0.871(10)	0.909(19)	0.861(10)	0.866(6)
60.256	66.069	0.836(16)	0.880(10)	0.841(17)	0.869(10)	0.865(6)
66.069	72.444	0.860(17)	0.897(10)	0.912(19)	0.873(10)	0.885(6)
72.444	79.433	0.866(17)	0.887(10)	0.914(19)	0.865(10)	0.879(6)
79.433	87.096	0.870(17)	0.868(10)	0.884(19)	0.872(10)	0.871(6)
87.096	95.499	0.875(17)	0.891(10)	0.864(18)	0.870(10)	0.878(6)
95.499	104.713	0.872(17)	0.900(11)	0.904(19)	0.898(11)	0.896(6)
104.713	114.815	0.870(17)	0.923(11)	0.926(20)	0.907(11)	0.910(7)
114.815	125.893	0.865(17)	0.922(11)	0.957(21)	0.888(11)	0.904(7)
125.893	138.038	0.851(17)	0.914(11)	0.912(20)	0.908(11)	0.902(7)

TABLE IV. (*Continued*.)

E_{low}	E_{high}	FIC	PPAC Perp.	PPAC tilted 1	PPAC tilted 2	$\langle n\_TOF \rangle$
138.038	151.356	0.882(18)	0.911(11)	0.922(21)	0.893(11)	0.902(7)
151.356	165.959	0.889(19)	0.903(11)	0.910(21)	0.933(12)	0.913(7)
165.959	181.970	0.893(19)	0.921(12)	0.960(22)	0.923(12)	0.922(7)
181.970	199.526	0.906(20)	0.903(12)	0.946(22)	0.922(12)	0.915(7)
199.526	218.776	0.865(19)	0.927(12)	0.947(23)	0.911(12)	0.914(7)
218.776	239.883	0.899(20)	0.924(13)	0.942(23)	0.937(12)	0.928(8)
239.883	263.027	0.924(22)	0.927(13)	0.948(23)	0.905(12)	0.920(8)
263.027	288.404	0.895(21)	0.934(13)	0.923(24)	0.939(13)	0.930(8)
288.403	316.227	0.869(21)	0.951(13)	0.943(24)	0.941(13)	0.934(8)
316.228	346.737	0.890(22)	0.954(14)	0.968(25)	0.920(13)	0.933(8)
346.736	380.189	0.919(22)	0.942(14)	0.982(26)	0.926(13)	0.936(8)
380.190	416.870		0.914(13)	0.951(25)	0.916(13)	0.919(9)
416.870	457.089		0.947(14)	0.976(27)	0.933(13)	0.944(9)
457.089	501.188		0.938(14)	0.963(26)	0.941(13)	0.943(9)
501.188	549.541		0.953(14)	0.990(28)	0.938(13)	0.950(9)
549.541	602.560		0.906(14)	0.937(27)	0.932(13)	0.922(9)
602.560	660.694		0.942(15)	1.004(29)	0.971(13)	0.962(9)
660.694	724.436		0.913(14)	0.984(29)	0.922(13)	0.924(9)
724.436	794.328		0.930(15)	1.019(30)	0.941(13)	0.944(9)
794.328	870.964		0.932(15)			0.932(15)
870.964	954.993		0.914(15)			0.914(15)

indicated by the solid line. We remind that for neutron energies below 20 MeV a wealth of data are available in the literature, with the standard cross sections of both isotopes characterized by an uncertainty of less than 1%. Therefore the very good agreement between n_TOF results and the ENDF/B-VII.1 evaluations, evident in Fig. 4, provides strong confidence in the accuracy of the new data, in particular in the systematic uncertainty related to the sample mass and in the efficiency corrections. Some minor differences can nevertheless be noticed in the figure, in particular around 12 MeV neutron energy, where the dip corresponding to a valley in the ^{238}U(n,f) cross section is less pronounced in the n_TOF dataset, relative to ENDF/B-VII.1 evaluation. Another minor difference can be observed around the ^{238}U fission threshold, slightly above 1 MeV. In this region, the n_TOF data are systematically shifted to higher energies, possibly indicating that the fission threshold in the evaluation needs to be increased by a small amount.

Figure 5 shows the results of the four different measurements at n_TOF, from 500 keV to 1 GeV (the data are reported in Table IV). The error bars on the symbols indicate only counting statistics uncertainties. Above 20 MeV some differences can be observed between the various results. In particular, the FIC results are systematically lower than all the PPAC ones. Among the PPAC data, the results obtained in the first measurement with the tilted configuration are systematically higher than the other two datasets, with the difference becoming more pronounced above ∼500 MeV. It should be noticed, however, that all differences are well within the combined uncertainties of the present results, related to independent systematic effects.

Each of the four datasets collected at n_TOF represents a new result by itself, and should be considered independently from each other, for example in re-evaluating the fission cross section ratio. Nevertheless, for the purpose of this paper it may
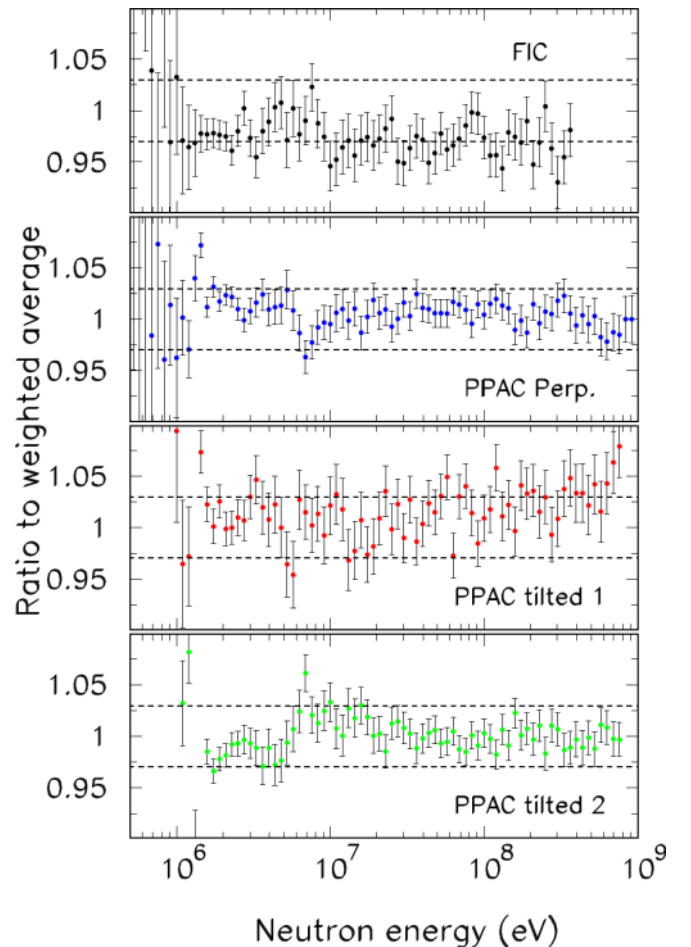

FIG. 6. (Color online) Ratio between the various datasets collected in the four measurements at n_TOF and their weighted average. The dashed lines represent the ±3% uncertainty limits.

be convenient to combine all four datasets. To this end, a weighted average was performed. Since the uncertainties due to systematic effects are similar in magnitude for the different datasets, only the uncorrelated uncertainties due to counting statistics were taken into account. The ratio obtained with this procedure can be more easily compared with data from previous measurements, as well as with evaluations and theoretical calculations. Moreover, it can be used to analyze the dispersion of the n_TOF datasets to draw further conclusions on their accuracy. This last point is illustrated in Fig. 6, which shows the divergence of the n_TOF results from their weighted average, as functions of neutron energy. Except for some details, the difference in all cases is within the ~3% systematic uncertainty associated with each dataset. (In the crude approximation adopted here, neglecting possible correlations between some datasets, the systematic uncertainty on the weighted average is around 1% up to 200 MeV, and between 1 and 2% above this energy.) This observation provides further strength on the accuracy of the present results.

Comparison with previous results, evaluations, and model predictions

The n_TOF fission cross section ratio discussed above is compared with the two major datasets extending to high energy in Fig. 7 (the data from Nolte *et al.* [7] are not shown because of their large uncertainties). Very good agreement is found with the data of Lisowski *et al.* [4] and with the current ENDF/B-VII.1 evaluation all the way up to 200 MeV, definitely ruling out the lower values reported by Shcherbakov *et al.* [6]. Above this value, the n_TOF data seem to maintain

a constant or slightly increasing trend, contrary to the data of Lisowski *et al.*, which seem to indicate the start of a decline in the higher energy points.

Some important information on the fission mechanism at high energy can be extracted from the comparison of the present data with the results of recent theoretical calculations of the fission cross sections of various actinides at high energy. More details on the calculations can be found in [24]. The aim of the work was to provide a way to estimate fission cross sections in the neutron energy range above 100 MeV, where no (or very few) reliable data exist. This is also the case for the fission cross section ratio discussed here. In the energy range 200 MeV–1 GeV considered in this work, model calculations were performed in order to estimate the absolute cross sections and, consequently, their ratio, to be compared with the present data. In Ref. [24], (*p,f*) and (*n,f*) cross sections were evaluated for both isotopes in the energy range 100 MeV–1 GeV using the intranuclear cascade code INCL++ [25] coupled to the evaporation-fission code GEMINI++ [26]. Two parameters in the fission model were optimized to reproduce the (*p,f*) cross sections measured in Ref. [27] from 200 MeV to 1 GeV (see Ref. [24] for details). The corresponding (*n,f*) cross sections were evaluated without further adjustment of model parameters, because the models already account for the observed differences in (*p,f*) and (*n,f*) cross sections around 200 MeV, while protons and neutrons are expected to have similar behavior with increasing incident energy and the fission cross sections to be of the same order of magnitude around 1 GeV. Such an assumption made it possible to reproduce also the (*n,f*) data from 100 MeV to 200 MeV, even if the conditions
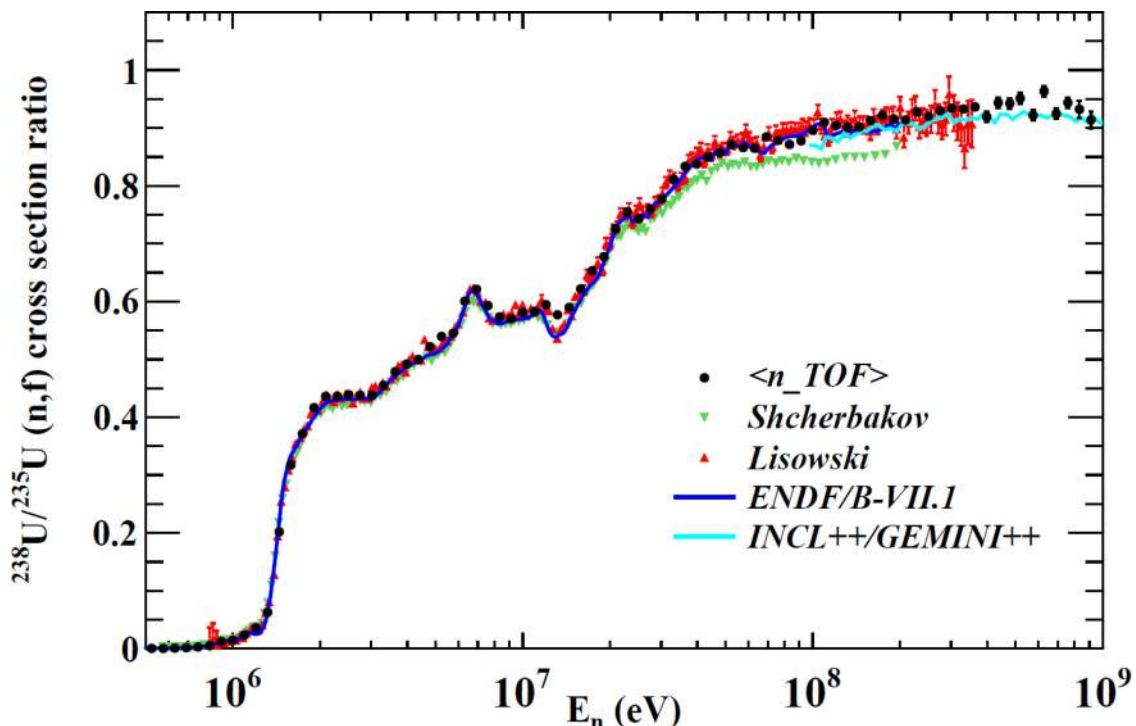

FIG. 7. (Color online) ^{238}U/^{235}U (*n,f*) cross section ratio obtained from the weighted average of the four n_TOF datasets compared with previous results from Refs. [4] and [6], with the ratio extracted from the ENDF/B-VII.1 library and with the results of model calculations from Ref. [24].
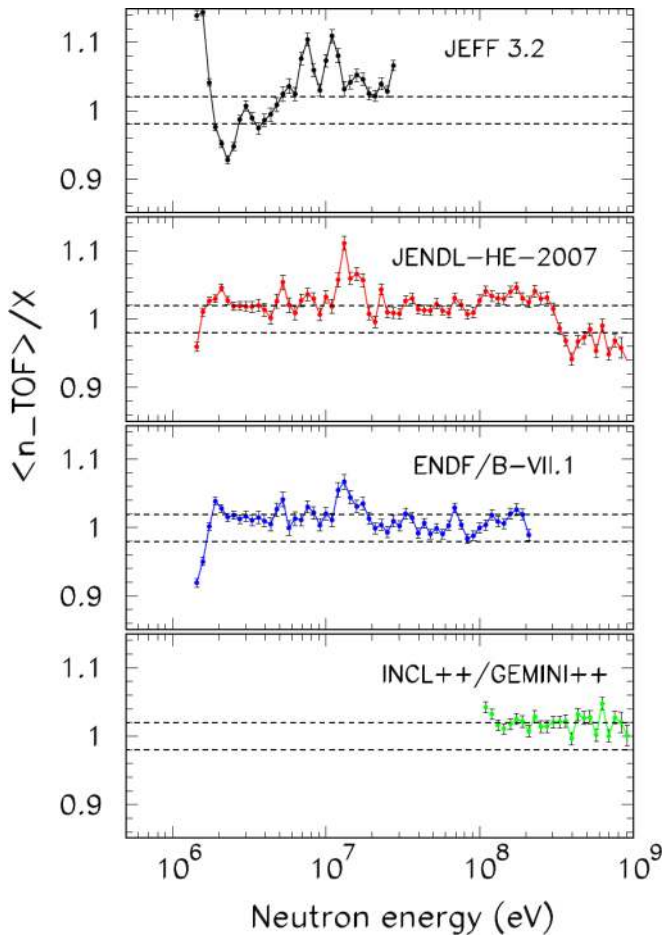
FIG. 8. (Color online) Deviation of the average n_TOF ^{238}U/^{235}U (n,f) cross section ratio from the predictions of the major evaluated nuclear data libraries and from the INCL++/GEMINI++ model calculations. The horizontal lines represent the limit of $\pm 2\%$ deviation.

of validity of the intranuclear cascade model are poorly satisfied at such relatively low energies. The theoretical cross sections are affected by statistical errors inherent in the Monte Carlo technique, which propagate to their ratios and have to be considered in the comparison with the experiment. The results of the model calculations, which are show in Fig. 7 by the light-blue curve, are in good agreement with present data at all energies. Although some systematic effects in the calculations may be at least partially compensated in the cross section ratio, the good agreement indicates that the theoretical treatment of Lo Meo *et al.* might be adequate for predicting the fission cross section of actinides above 100 MeV neutron energy.

More evidences in this respect could come from additional fission studies at n_TOF up to 1 GeV.

A more quantitative comparison between the ^{238}U/^{235}U fission cross section ratio measured at n_TOF and evaluations or model calculation is shown in Fig. 8. For completeness, the present results are also compared with the libraries JEFF3.2 and JENDL-HE-2007 [5]. While the former contains data only up to 30 MeV, the latter extends up to 3 GeV, being in fact the only library reporting evaluated cross sections above 200 MeV. While ENDF/B-VII.1 and the INCL++/GEMINI++ predictions agree, within 2%, with the present result, a relatively large difference exists with respect to the JEFF3.2 library, in the whole energy region from threshold to 30 MeV. A reasonable agreement is observed relative to JENDL-HE-2007 at all energies, although a strange behaviour is observed around $\sim$300 MeV, with the ratio of the evaluated cross sections suddenly increasing above this energy. A final consideration can be made regarding the energy region around the fission threshold of ^{238}U. A difference is observed relative to all major libraries, although not always in the same direction, possibly indicating a slight under- or overestimate of the threshold energy.

IV. CONCLUSIONS

The ^{238}U/^{235}U fission cross section ratio has been measured at n_TOF, for the first time up to 1 GeV, with two different detection systems, one of which was used in two different geometrical configurations. The results of the measurements agree with each other within the estimated systematic uncertainty of approximately 3%. Furthermore, the results are in all cases in agreement with evaluated cross sections and standard values between 0.5 and 20 MeV, thus providing confidence in their accuracy. The results have been combined in order to obtain a unique dataset for comparison with previous results and evaluations, up to 200 MeV, and with theoretical calculations based on the intranuclear cascade model coupled with an evaporation-fission code, all the way up to 1 GeV. The extracted ratio rules out the results of Shcherbakov *et al.*, and is in very good agreement both with ENDF/B-VII.1 evaluation, up to 200 MeV, and with theoretical calculations up to 1 GeV. Some differences are instead observed between present data and other major libraries. These results could be used to improve the accuracy of current libraries, and in particular of the standard used in a variety of applications.

[1] A. Carlson *et al.*, Nucl. Data Sheets **110**, 3215 (2009).

[2] https://www-nds.iaea.org/standards/Data/endf-6-format/std-092_U_235.endf.

[3] http://www-nds.iaea.org/standards/Data/endf-6-format/std-092_U_238.endf .

[4] P. Lisowski, A. Gavron, W. E. Parker, S. J. Balestrini, A. D. Carlson, O. A. Wasson, and N. W. Hill, *Proceedings of the International Conference on Nuclear Data for Science and Technology, May 13-17 1991, Julich, Germany* (Springer-Verlag, Berlin, Heidelberg, 1992), p. 732 .

[5] https://www-nds.iaea.org/exfor/endf.htm.

[6] O. Shcherbakov *et al.*, J. Nucl. Sci. Technol. **39**, 230 (2002).

[7] R. Nolte, M. S. Allie, F. D. Brooks, A. Buffler, V. Dangendorf, J. P. Meulders, H. Schuhmacher, F. D. Smit, and M. Weierganz, Nucl. Sci. Eng. **156**, 197 (2007).

[8] https://ntof-exp.web.cern.ch/ntof-exp/.

[9] U. Abbondanno *et al.*, CERN/INTC-O-011 INTC-2002-037, CERN-SL-2002-053 ECT (2003).

[10] C. Guerrero *et al.*, Eur. Phys. J. A **49**, 27 (2013).

[11] M. Barbagallo *et al.*, Eur. Phys. J. A **49**, 156 (2013).

[12] N. Colonna *et al.*, Energy Environ. Sci. **3**, 1910 (2010).

[13] M. Calviani *et al.*, Nucl. Instrum. Methods Phys. Res., Sect. A **594**, 220 (2008).

[14] M. Calviani *et al.*, Phys. Rev. C **80**, 044604 (2009).

[15] T. T. Böhlen, F. Cerutti, M. P. W. Chin, A. Fassò, A. Ferrari, P. G. Ortega, A. Mairani, P. R. Sala, G. Smirnov, and V. Vlachoudis, Nucl. Data Sheets **120**, 211 (2014).

[16] C. Paradela *et al.*, Phys. Rev. C **82**, 034601 (2010).

[17] D. Tarrío *et al.*, Nuclear Instrum. Methods Phys. Res., Sect. A **743**, 79 (2014).

[18] C. Paradela, I. Duran, D. Tarrío, L. Audouin, L. Tassan-Got, and C. Stephan, *Proceedings of the 2nd International Conference on Advancements in Nuclear Instrumentation Measurement Methods and their Applications (ANIMMA), June, 2011, Ghent, Belgium* (IEEE, Ghent, 2011), pp. 6–9.

[19] D. Tarrío *et al.*, Nucl. Data Sheets **119**, 35 (2014).

[20] D. Tarrío *et al.*, Phys. Rev. C **83**, 044620 (2011).

[21] https://www-nds.iaea.org/exfor/exfor.htm.

[22] D. Tarrío, Ph.D. thesis, Universidade de Santiago de Compostela, Spain, 2012.

[23] L. S. Leong and L. Tassan-Got, Ph.D. thesis, University of Paris, France, 2013.

[24] S. Lo Meo, D. Mancusi, C. Massimi, G. Vannini, and A. Ventura, Nucl. Phys. A **933**, 43 (2015).

[25] A. Boudard, J. Cugnon, J.-C. David, S. Leray, and D. Mancusi, Phys. Rev. C **87**, 014606 (2013).

[26] D. Mancusi, R. J. Charity, and J. Cugnon, Phys. Rev. C **82**, 044610 (2010).

[27] A. Kotov *et al.*, Phys. Rev. C **74**, 034605 (2006).